Title
Copper-transporting P-type ATPases use a unique ion-release pathway

Journal
Nature Structural & Molecular Biology, 21(1)

ISSN
1545-9993

Authors
Andersson, Magnus
Mattle, Daniel
Sitsel, Oleg
et al.

Publication Date
2014

DOI
10.1038/nsmb.2721

Peer reviewed

Published in final edited form as:
Nat Struct Mol Biol. 2014 January ; 21(1): 43–48. doi:10.1038/nsmb.2721.

Copper-transporting P-type ATPases use a unique ion-release pathway

Magnus Andersson[1,*,#], **Daniel Mattle**[2,*], **Oleg Sitsel**[2], **Anna Marie Nielsen**[2], **Stephen H. White**[1], **Poul Nissen**[2], and **Pontus Gourdon**[2]

[1]Department of Physiology and Biophysics, University of California at Irvine, Irvine, CA 92697-4560, USA

[2]Centre for Membrane Pumps in Cells and Disease - PUMPKIN, Danish National Research Foundation, Aarhus University, Department of Molecular Biology and Genetics, Gustav Wieds Vej 10C, DK-8000 Aarhus C, Denmark

Abstract

Heavy metals in cells are typically regulated by P_{IB}-type ATPases such as the copper transporting Cu^+-ATPases. The first crystal structure of a Cu^+-ATPase (LpCopA) was trapped in a transition state of dephosphorylation ($E2.P_i$) and inferred to be occluded. The structure revealed a P_{IB}-specific topology and suggested a copper transport pathway across the membrane. Here we show by molecular dynamics (MD) simulations that extracellular water solvates the transmembrane (TM) domain, indicative of a pathway for Cu^+ release. Furthermore, a new LpCopA crystal structure determined at 2.8 Å resolution, trapped in the E2P state (which is associated with extracellular exchange in P_{II}-type ATPases), delineates the same conduit as also further supported by site-directed mutagenesis. The E2P and $E2.P_i$ states therefore appear equivalent and open to the extracellular side, in contrast to P_{II}-type ATPases where the $E2.P_i$ state is occluded. This indicates that Cu^+-ATPases couple dephosphorylation differently to the conformational changes associated with ion extrusion. The ion pathway may explain why Menkes' and Wilson's disease mutations at the extracellular side impair protein function, and points to an accessible site for novel inhibitors targeting Cu^+-ATPases of pathogens.

Class IB P-type ATPases (P_{IB}-type ATPases) perform active transport of heavy metals across cellular membranes and are of crucial importance for heavy metal homeostasis[1–3]. The Cu^+-ATPase subclass (CopA), the most widespread among P_{IB}-type ATPases, has attracted particular attention, because malfunction of the human members ATP7A and ATP7B is the direct cause of the severe Menkes' and Wilson's diseases, respectively[4,5]. To understand the mechanisms of heavy-metal transport and disease, the transport pathway and how it is coupled to the ATPase reaction cycle must be described. The mechanistic view of how P-type ATPases mediate ion flux over the membrane has emerged primarily from studies of P_{II}-ATPases, such as the sarco(endo)plasmic reticulum Ca^{2+}- ATPase

[*]contributed equally

[#]Magnus Andersson's present address is Science for Life Laboratory, Department of Theoretical Physics, Swedish e-Science Research Center, KTH Royal Institute of Technology, SE-171 21 Solna, Sweden

AUTHOR CONTIBUTIONS

M.A. performed MD simulations, D.M., O.S. and A.M.N. established DNA constructs, D.M. and O.S. performed the protein purifications, O.S. activity measurements, D.M. crystallized, processed data and solved the crystal structures guided by P.N. and P.G. and all authors analyzed results. M.A. and P.G. designed the project supervised by S.H.W. and P.N., M.A., D.M. O.S. and P.G. generated figures, and all authors contributed to the writing of the paper.

COMPETING FINANCIAL INTERESTS

The authors declare no competing financial interests.

(SERCA)[6–13] (Fig. 1a): An E1 state binds intracellular ions with high-affinity, followed by occlusion and phosphorylation (E1P), which triggers conformational changes and access to the extracellular environment (E2P). The ions are then unloaded and extracellular counter-ions (protons for SERCA) bind and stimulate re-occlusion and dephosphorylation ($E2.P_i$). Release of bound phosphate yields the fully dephosphorylated conformation (E2), which then shifts into the inward-facing conformation (E1) to initiate a new reaction cycle. However, it is not clear whether a similar E1/E2 reaction scheme applies to other classes of P-type ATPases, particularly those for which counter-transport may not apply, such as the P_{IB}-ATPases[14].

Recently, the structure of a Cu^+-exporting P_{IB}-type ATPase from *Legionella pneumophila* (LpCopA) was determined in a Cu^+-free transition state of dephosphorylation ($E2.P_i$), as mimicked by AlF_4^-. The structure demonstrated a preserved P-type ATPase core structure with intracellular A- (actuator), P- (phosphorylation), and N- (nucleotide binding) domains and a transmembrane (TM) domain. Thus, phosphorylation and dephosphorylation regions in CopA are similar to those of SERCA. Moreover, putative Cu^+-sites of intracellular entry at Met148 (LpCopA numbering), internal coordination (involving the ^{382}Cys-Pro-Cys motif), and extracellular exit (at Glu189), suggested a three-stage transport pathway, which would be sensitive to conformational changes as observed for P_{II}-ATPases[15]. However, the intramembrane ion-binding cluster of CopA[16] lacks carboxylate residues, while in SERCA the equivalent region encompasses several negatively charged residues that participate in both calcium transport and H^+-counter-transport[8–13,17]. Furthermore, the CopA topology is considerably different, because of the presence of P_{IB}-specific helices MA and MB, and the absence of helices M7 through M10 associated with the P_{II}-ATPase (Supplementary Fig. 1). Cu^+ transport is therefore likely to operate through a class-specific mechanism. In the present study, we show this indeed to be the case, because dephosphorylation of LpCopA is not coupled to occlusion at the extracellular side of the TM domain, unlike for the P_{II}-type ATPases. MD simulations, X-ray crystallography, and mutational studies reveal a class-specific ion release pathway. These results may also explain why multiple Menkes' and Wilson's disease mutations are found in the homologous region of the human ATP7A and ATP7B transporters.

RESULTS

MD simulations suggest the $E2.P_i$ state to be open to the extracellular side

By means of a molecular dynamics (MD) simulation of the LpCopA $E2.P_i$ structure embedded in a dioleoylphosphocholine (DOPC) lipid bilayer, we searched the TM domain for ion pathways linking the three suggested points of Cu^+ binding. Surprisingly, we observed extracellular bulk water solvating the putative exit site region at Glu189, occasionally reaching as far as the intramembranous copper binding residues Cys382, Cys384, and Met717 (Fig. 1b, c and Supplementary Movie 1). The open $E2.P_i$ state hints at a class-specific release mechanism distinct from the one observed for SERCA, where the corresponding state is closed (Fig. 1a). Moreover, the extrusion pathway, which includes TM helices M2 (with Glu189), M6, and the P_{IB}-specific N-terminal MA (Supplementary Fig. 1)[2], appears to be unique.

Crystal structure of the E2P state

The results of the MD simulation led us to crystallize LpCopA in a copper-free E2P state using the phosphate analogue BeF_3^-, which in SERCA would yield the phopshoenzyme state that exposes the extracellular/luminal release pathway[13]. The structure, determined at 2.8 Å resolution (Fig. 2a and Table 1), revealed a configuration of the intracellular domains that is similar to the E2P conformation of SERCA (Fig. 2b and Supplementary Fig. 2) in

which the TGE-loop of the A-domain interacts with the phosphorylated Asp426 (mimicked by E2:BeF_3^-, Supplementary Fig. 3) but is not primed for dephosphorylation. However, in contrast to SERCA where the release pathway is controlled by helices M1-M2 and M3-M4 switching from open to occluded relative to M5-M10 along with dephosphorylation[13] ($RMSD_{backbone}$ 1.7 Å, Fig. 3a and Supplementary Fig. 4), the TM-domain of LpCopA remains almost unchanged in the E2P to E2.P_i transition ($RMSD_{backbone}$ 0.6 Å, Fig. 3b and Supplementary Fig. 4–5). This observation is strengthened by the fact that two independent crystal forms of the E2P conformation show similar structures (Supplementary Figs. 6–7 and Table 1).

The crystal structures and simulations outline the same Cu^+-transfer pathway

Interestingly, multiple crystal waters in the new E2P structure delineate a pathway (Fig. 2a, c) lined by transmembrane helices MA, M2, and M6, which coincides with the hydration patterns derived from MD simulation of the E2.P_i structure. This extracellular water cleft was also reproduced in a MD simulation of the E2P structure (Fig. 4, Supplementary Fig. 8 and Supplementary Movies 1–2). Our combined data therefore indicate that the E2.P_i and E2P conformations of LpCopA are both and equally open towards the extracellular side with water reaching the ion-binding sites deep in the TM domain. At the same time, the protein remains closed towards the intracellular side as required for an alternating access mechanism[18]. Can this pathway accommodate Cu^+ transport? An outline of the pore radii in LpCopA from the high-affinity ion-binding cluster to the extracellular side, show that both the crystal structures and the simulated average structures are open with respect to the size of Cu^+ ions[19], thus allowing transfer (Fig. 3c, Supplementary Fig. 9). Similar analyses of SERCA display an open E2P state in agreement with ion extrusion (Supplementary Fig. 10), while no pores were found for the E2.P_i state, in accordance with a Ca^{2+}-occluded state. Next, we simulated ion release for a Cu^+ ion positioned between the intramembranous high-affinity ligands Cys382 and Met717 and no major energy barriers were detected along the pathway (Supplementary Fig. 11). Even though the force was applied strictly perpendicular to the membrane, the ion followed the predicted release pathway, involving a 10 Å traverse movement in the membrane plane.

MD simulations and the E2P structure indicates an intramembranous Cu^+ site

Comparison of the crystal structure and MD simulations reveal additional details of the exit pathway, including preferred locations for water molecules. Two crystallographic water molecules were located adjacent to critical residues implicated in high-affinity copper binding and contributed to continuously occupied water pockets in the E2P simulation. Intriguingly, water pockets were also found at similar locations in the E2.P_i simulation, formed by water molecules with relatively long residence times (>15 ns, Supplementary Fig. 12) that entered from the extracellular milieu. Crystal waters and simulated water dynamics have been observed earlier to probe potential ion-binding sites[20,21] and, remarkably, the internal water pockets in the simulations correspond by structural alignment to calcium site I of the occluded [Ca_2]E1P conformation of SERCA (Fig. 4a and Supplementary Fig. 8, green spheres). Therefore, the internal water pockets hint at a role of this site in copper binding.

Residues along the observed conduit are critical for function of Cu^+-ATPases

To validate further the proposed ion conduit and mechanisms involved, we performed *in vitro* activity measurements of CopA point mutants using a well-established ATPase assay[22] (Fig. 4c and Supplementary Fig. 13 and Supplementary Tables 1 and 2). This analysis shows that Met717 is crucial for function, and that both side chain size and charge are important for Glu189, which in the human copper pumps is conserved as an aspartate. A significantly reduced activity for the Ala714Thr mutation is explained by direct steric hindrance of the

observed pathway. Furthermore, although Met100 and Met711 both are positioned at the proposed exit site, only Met711 displays mutational sensitivity, which is consistent with the peripheral locations of Met100 and M711 relative to the pathway, Met100 being the most distant (Supplementary Fig. 14). All considered, the release pathway is supported by mutational effects as probed by the ATPase activity and provides a possible basis for the impaired copper-transport function resulting from previously perplexing missense mutations associated with Menkes' and Wilson's diseases that are located in the vicinity of the extracellular cleft marked by MA, M2 and M6[15,23] (Supplementary Fig. 15). Consistent with our findings, the extracellular loop connecting MA and MB has been implicated in copper discharge in the human copper pump ATP7A[24].

Conserved prolines may control Cu^+ release

Interestingly, the E2.P_i MD simulation showed a shift of 3–5 Å of the extracellular ends of transmembrane helices MA and M6 originating from the well-conserved Pro94 and Pro710, respectively (Fig. 4b and Supplementary Fig. 16), suggesting that these residues may be involved in opening the release pathway to the exit site at Glu189. In agreement with this notion, we find the Pro94Ala and Pro710Ala mutations to impair CopA activity using the *in vitro* assay (Fig. 4c and Supplementary Tables 1 and 2). Moreover, MD simulations of the proline mutants showed significantly distorted hydration patterns providing a structural explanation for the observed phenotypes. For the Pro710Ala mutant, a misdirected pathway was predicted (Supplementary Fig. 17). In the Pro94Ala simulation, the pathway from Glu189 was largely maintained, but the water pockets at the intramembranous ion-binding ligands were less hydrated (Supplementary Fig. 17). Together, the *in vitro* data and the accompanying simulations are in support of Pro710 and Pro94 as key players in control of the release mechanism. Thus, while the intracellular segment of helix MB appears critical for copper uptake[15], an ion-extrusion function can be attributed to the extracellular part of MA (including Pro94), which is well-conserved in Cu^+-ATPases[15] (Supplementary Fig. 18).

The exit pathway is physiologically relevant

To investigate the physiological significance of the proposed release pathway and mutations, we assessed the CopA mutations *in vivo* by LpCopA complementation of a CopA-deficient *E. coli* strain using LpCopA constructs controlled by the CopA promotor of the host (Fig. 4c and Supplementary Fig. 19). A possible caveat with this approach is that extracellular Cu^+-accepting partners may be missing or incapable of recognizing the recombinant ATPase. However, because the Asp426Asn dead-mutant (with an inactivated catalytic phosphorylation site) and wild-type LpCopA were observed to switch the copper tolerance of the *E. coli* strain, the assay can be used as a proxy for functional Cu^+ transport *in vivo*. Overall, the general trends from ATPase activities *in vitro* are reproduced *in vivo*, albeit less pronounced (Fig. 4c). Strikingly however, the two most potent mutations of the region *in vitro*, Ala714Thr, which sterically blocks the conduit, and Pro710Ala also display a remarkable susceptibility to copper *in vivo*, substantiating the relevance of the release pathway for CopA copper transport in cells.

DISCUSSION

The combined results from our experiments and simulations map a unique release pathway available in Cu^+-transporting P_{IB}-type ATPases, which is similarly hydrated in the E2P and E2.P_i states. The structural boundaries and chemical characteristics of this pathway as well as the actual release mechanism appear unique to P_{IB}-type ATPases. By analogy to SERCA[17], the CopA transport mechanism might also involve counter-ions such as protons. However, so far counter-ion requirements have not been observed for any P_{IB}-type ATPase. Protons would be the obvious candidate, but a current observed for the human copper

transporter ATP7B is pH-insensitive[25,26]. The unexpected open configuration of the E2.P_i structure also disfavors the requirement of counter-ions, because dephosphorylation of LpCopA is not tightly coupled to occlusion of the TM-domain, as would be expected for an active countertransport (Fig. 5). Further supporting a distinctly tuned reaction cycle for Cu^+-ATPases, the ATP-induced phosphoenzyme formation has been observed in the absence as well as in the presence of the transported ion, unlike for SERCA[27]. These unique features accompanying P_{IB}-ATPase function can be explained in terms of the significant structural differences between P_{II} and P_{IB}-ATPases. For instance, the A-domain-M1 linker that controls the Ca^{2+} entry region in P_{II}-ATPases is lacking in CopA. Furthermore, CopA also lacks the M7-M10 bundle, which in P_{II}-ATPases (SERCA and Na^+, K^+-ATPase) contains a solvated channel in the E2 and E2.P_i states that presumably supports proton exchange[28] (Supplementary Figs. 1 and 20–21). Differentiation may also apply to the P_{IB}-ATPases; the MA helix in Zn^{2+} and Co^{2+}-ATPases (Supplementary Figs. 18 and 22) is lacking the corresponding Pro94 and the extracellular portion is less conserved compared to Cu^+-ATPases. Notably, distinct mechanisms within subfamilies are also observed for e.g. ABC-transporters[29].

Our E2P crystal structure and MD simulations of LpCopA in combination with mutational analyses suggest a unique release mechanism for Cu^+ P_{IB}-type ATPases. The extracellular release pathway is possibly involved in specific and controlled delivery to Cu^+ acceptor chaperones[30], preventing detrimental effects of free copper in the extracellular space, or to other cupro-proteins that need the ion for function[31,32]. The pathway further explains why Menkes and Wilson mutations in this region impair ATP7A/B function. The high prevalence and critical function of P_{IB}-genes against intra-phagolysosomal copper defence for pathogenic bacteria[33,34] and the mutation-sensitivity of the exit pathway point to a site for inhibitors with favorable access from the outside of the cells, similar to cardiotonic steroids and omeprazole, which are clinically used inhibitors of Na^+, K^+-ATPase and H^+, K^+-ATPase.

ONLINE METHODS

Sample preparation

LpCopA mutants were generated using Agilent Technologies' QuikChange Lightning site-directed mutagenesis kit using the full-length non-tagged *lpg1024* gene in pET22b(+). Cell growth to solubilization in the detergent $C_{12}E_8$ (octaethylene glycol monododecyl ether) and ultracentrifugation were conducted as described previously[15]. For crystallization, the sample was further purified according to this protocol, while each construct for *in vitro* characterization was loaded onto a separate pre-equilibrated 5 ml affinity column, either GE Healthcare HisTrap HP or Qiagen Ni-NTA Superflow Cartridge, washed with 20 mM Tris-HCl pH=7.6, 200 mM KCl, 1 mM $MgCl_2$, 20% glycerol, 5 mM BME and 0.28 mM $C_{12}E_8$, and eluted with 500 mM imidazole. The buffer of the concentrated protein was thereafter exchanged using a GE Healthcare HiTrap Desalting column to 20 mM MOPS-KOH pH=6.8, 80 mM KCl, 1 mM $MgCl_2$, 20% glycerol, 5 mM BME and 0.28 mM $C_{12}E_8$. The constructs were concentrated and the purity estimated using SDS-PAGE. To assess relative protein concentrations, the intensity of individual LpCopA bands at ~75 kDa were quantified using the software ImageJ[37]. A second SDS-PAGE gel (Supplementary Fig. 13) was generated using equal protein amounts as calculated from the first gel. The protein concentration of the D426N mutant was determined using light absorbance at 280 nm and used as reference in the activity assay (see below).

In vitro characterization

The Baginski method with arsenic detection under aerated conditions was used to assess ATPase activity[22]. Measurements were conducted using equal amounts of protein for each construct as judged by ImageJ (and shown in Supplementary Fig. 13), corresponding to 3.8 μM for D426N, 40 mM MOPS-KOH pH=6.8, 150 mM NaCl, 5 mM KCl, 5 mM $MgCl_2$, 20 mM $(NH4)_2SO_4$, 20 mM L-cysteine, 5 mM NaN_3, 0.25 mM Na_2MoO_4, 1.2 mg/ml L-α-phosphatidylcholine lipids from soybean and 3.7 mM $C_{12}E_8$ in a total volume of 50 μl. 10 μM ammonium tetrathiomolybdate was added to prevent activity from background copper contaminants, and the protein was incubated for 15 minutes with 1 mM $CuCl_2$ (reduced to Cu^+) Reactions were started by addition of 4.8 mM ATP, incubated at 37 °C with shaking for 25 minutes and stopped by adding 50 μL of freshly made stop-solution (0.083 % SDS, 417 mM HCl, 142 mM L-ascorbic acid, 4.72 mM $(NH_4)_6Mo_7O_{24}•4H_2O$). After 10 minutes of incubation at 19 °C, 75 μL stabilizing solution (154 mM $NaAsO_2$, 68 mM $Na_3C_6H_5O_7•2H_2O$, 349.4 mM CH_3COOH) was added and incubated for 30 minutes at 19 °C. Absorbance was measured at 860 nm using a PerkinElmer VICTOR3 multilabel plate counter. The raw output data (Supplementary Table 1) was thereafter scaled (Supplementary Table 2) to account for the subtle variations in the relative intensities of Supplementary Fig. 13. These data were then plotted on a scale of 100 % (wild-type LpCopA activity) to 0 % (D426N mutant activity), through removal of the background of the D426N dead mutant, and displayed in Fig. 4c. One experiment with nine replicates was done for the *in vitro* activity data. To assess the reproducibility of our assay, two mutations were tested using an additional independent experiment (Supplementary Fig. 23).

In vivo characterization

E. coli CopA-deleted strain CN2328, as well as its progenitor strain CN1709 and the plasmid pCN2345 containing the native *E. coli* CopA promoter and gene were obtained from Lisbeth Birk Møller[38]. pCN2345 was mutated to allow replacement of *E. coli* CopA with LpCopA with maintained promoter and wild-type and mutants of LpCopA incorporated separately. The plasmids were then transformed into CN2328 and an empty pET22b(+) vector was transformed into CN1709 cells and used as a control. Pre-cultures were grown overnight and their OD_{600nm} were adjusted to 1.0 prior to inoculation. 10 μl of cells were used to inoculate 190 ul of LB media with 100 ug/ml ampicillin and $CuCl_2$ concentrations adjusted to 0 and 3 mM. The inoculated media were grown in 96-well plates in a shaking incubator at 37 °C, and OD_{560nm} was measured in hourly intervals using a PerkinElmer VICTOR3 multilabel plate counter. The growth curves of the cells at different $CuCl_2$ concentrations are shown in Supplementary Fig. 19 and the final time point for 3 mM $CuCl_2$ is shown in Fig. 4c. Three independent experiments were conducted, with three replicates each for experiment 1 and 3 and 15 replicates for experiment 2. The averaged value of the averages for each mutant in every independent experiment at the final time point for 3 mM $CuCl_2$ was used in Fig. 4c, and wild-type LpCopA activity was set as 100 %. Error bars were calculated by using three data points per mutant per experiment. The three data points of experiment 2 were selected by taking the lowest, highest and most average value for each mutant from the 15 replicates.

Crystallization, Data collection and Model building

Crystallization of the LpCopA E2-BeF_3^- complex (E2P like state) was performed by hanging drop vapor diffusion. 0.15 ml 10 mg/ml LpCopA was re-lipidated for 16h according to the HiLiDe method[39] using 0.5 mg Dioleoyl-phosphatidylcholine (DOPC) and between 5–12 μl 100 mg/ml $C_{12}E_8$. The sample was centrifuged for 10 min at 100,000*g* and incubated with 10 mM NaF, 3.2 mM EGTA, 10 μM ammonium-tetrathiomolybdate (TTM) and 2 mM $BeSO_4$. Best crystals (in the space group C2) were found after two days with 5

mM β-NAD in the protein solution and a precipitant solution containing 10% glycerol, 200 mM KCl, 3% t-BuOH, 14% PEG 2K MME and 5 mM BME mixed 1:1 with the protein solution. The $P2_12_12_1$ crystal form, displaying a different packing, grew by addition of 36.7 mM Fos-Choline®10 to the protein solution. Screening of diffraction properties was conducted at Maxlab, SLS and ESRF and final data were collected at ID29 at ESRF using a pixel detector (Pilatus 6M) and scaled using XDS[40]. Initial phases were obtained by molecular replacement using Phaser[41] with the E2-AlF_4^- structure of LpCopA (pdb-id: 3RFU) as a search model. Iterative refinement and model building were performed with Phenix[42] and the molecular graphics program Coot[43]. The low resolution E2:BeF_3^- structure ($P2_12_12_1$ crystal form) was determined using Phaser with the above high resolution structure as a search model (pdb-id: 4BBJ) and subjected to rigid body refinement in Phenix[44]. Structures were analyzed using Molprobity.

Building the MD systems

For the E2.P_i state (based on the E2:AlF_4^- structure, pdb-id: 3RFU, chain A) and E2P state (E2:BeF_3^-, pdb-id: 4BBJ), protein with ligands were inserted into the lipid bilayer by aligning the centers-of-mass of the TM-region and a 500 molecule DOPC bilayer (built using the CHARMM-GUI membrane builder[45], and solvated in excess water[46]. Alternative docking methods give similar insertion depths[47,48] (Supplementary Fig. 24). Electric neutrality was achieved by addition of 7 and 9 Na^+ counter-ions to the E2.P_i and E2P system, respectively. The E2.P_i Pro94Ala and Pro710Ala mutants, generated using the VMD plugin psfgen[49], were constructed in a similar fashion.

MD simulation

Following a 10,000-step conjugate-gradient energy minimization and gradual heating from 0 to 310 K over 120 ps, two consecutive 1 ns simulations at constant temperature (310 K) and volume (NVT ensemble) equilibrated lipids and water molecules, respectively. The protein was then progressively released from its initial configuration over seven 1 ns simulations, followed by a production run at constant temperature (310 K) and pressure (1 atm) (NPT ensemble). The production runs for wild-type, P94A, and P710A E2.P_i states were 100 ns, while the E2P state was 85 ns. Molecular dynamics simulations were run with the NAMD 2.7 software package[46,50]. The CHARMM22 including CMAP correction and CHARMM36 force fields[51,52] were used for protein and lipids, respectively, and the TIP3P model was used for the water molecules[46]. A time step of 1 fs was used to integrate the equations of motion, and a reversible multiple time step algorithm[53] of 4 fs was used for the electrostatic forces and 2 fs for short-range, non-bonded forces. The smooth particle mesh Ewald method[54,55] was used to calculate electrostatic interactions. The short-range interactions were cut off at 12 Å. All bond lengths involving hydrogen atoms were held fixed using the SHAKE[56] and SETTLE[57] algorithms. A Langevin dynamics scheme was used for thermostating and Nosé-Hoover-Langevin pistons were used for pressure control[58,59]. Molecular graphics and simulation analyses were generated with the VMD 1.8.7 software package[49]. The evolution of the simulation cell dimensions shows the simulations to equilibrate within 20 ns (Supplementary Fig. 25). The rmsd for the E2.P_i state simulations were relatively high (>4 Å), while the E2P state was less flexible with an rmsd of ~2 Å (Supplementary Fig. 26). The relatively high RMSD values for the E2.P_i state simulations stemmed from the large soluble headpiece, since the TM domain displayed substantial stability, reaching a plateau at ~2 Å after 20 ns. To account for the underlying structural factors for the large RMSD, we measured the evolution of the centers-of-mass (COM) for the A/N/P domains (Supplementary Fig. 27). We note significant COM stability in all dimensions for the individual domains and conclude that the large RMSD stems from inherent flexibility of the domains and loop regions, rather than rigid body motions. The

procedure for calculating the potential of mean force (PMF) associated with ion release is described in the Supplementary Information.

Supplementary Material

Refer to Web version on PubMed Central for supplementary material.

Acknowledgments

We thank Dr. Lisbeth Birk Møller for providing the strains and plasmid required for the *in vivo* complementation assay, T. Klymchuk for technical assistance as well as J. L. Karlsen for support on crystallographic computing. M.A. was supported in part by a Senior Postdoctoral Fellowship from the Branches Cost-Sharing Fund from the Institute of Complex Adaptive Matter ICAM supported in part by the National Science Foundation. The research was also supported by NIH grants GM074637 and GM086685 to S.H.W. D.M. and O.S. are supported by the Graduate School of Science and Technology at Aarhus University. P.N. was supported by an advanced research grant (Biomemos) of the European Research Council. MD simulations were supported in part by the National Science Foundation through TeraGrid (now Xsede) resources provided by the Texas Advanced Computing Center at the University of Texas at Austin.

References

1. Lutsenko S, Kaplan JH. Organization of P-type ATPases: significance of structural diversity. Biochemistry. 1995; 34:15607–13. [PubMed: 7495787]
2. Kuhlbrandt W. Biology, structure and mechanism of P-type ATPases. Nat Rev Mol Cell Biol. 2004; 5:282–95. [PubMed: 15071553]
3. Arguello JM, Eren E, Gonzalez-Guerrero M. The structure and function of heavy metal transport P1B-ATPases. Biometals. 2007; 20:233–48. [PubMed: 17219055]
4. Vulpe C, Levinson B, Whitney S, Packman S, Gitschier J. Isolation of a candidate gene for Menkes disease and evidence that it encodes a copper-transporting ATPase. Nat Genet. 1993; 3:7–13. [PubMed: 8490659]
5. Bull PC, Thomas GR, Rommens JM, Forbes JR, Cox DW. The Wilson disease gene is a putative copper transporting P-type ATPase similar to the Menkes gene. Nat Genet. 1993; 5:327–37. [PubMed: 8298639]
6. Albers RW. Biochemical aspects of active transport. Annu Rev Biochem. 1967; 36:727–56. [PubMed: 18257736]
7. Post RL, Hegyvary C, Kume S. Activation by adenosine triphosphate in the phosphorylation kinetics of sodium and potassium ion transport adenosine triphosphatase. J Biol Chem. 1972; 247:6530–40. [PubMed: 4263199]
8. Toyoshima C, Nakasako M, Nomura H, Ogawa H. Crystal structure of the calcium pump of sarcoplasmic reticulum at 2.6 A resolution. Nature. 2000; 405:647–55. [PubMed: 10864315]
9. Toyoshima C, Nomura H. Structural changes in the calcium pump accompanying the dissociation of calcium. Nature. 2002; 418:605–11. [PubMed: 12167852]
10. Toyoshima C, Mizutani T. Crystal structure of the calcium pump with a bound ATP analogue. Nature. 2004; 430:529–35. [PubMed: 15229613]
11. Olesen C, Sorensen TL, Nielsen RC, Moller JV, Nissen P. Dephosphorylation of the calcium pump coupled to counterion occlusion. Science. 2004; 306:2251–5. [PubMed: 15618517]
12. Sorensen TL, Moller JV, Nissen P. Phosphoryl transfer and calcium ion occlusion in the calcium pump. Science. 2004; 304:1672–5. [PubMed: 15192230]
13. Olesen C, et al. The structural basis of calcium transport by the calcium pump. Nature. 2007; 450:1036–42. [PubMed: 18075584]
14. Mattle D, et al. On Allosteric Modulation of P-Type Cu-ATPases. J Mol Biol. 2013
15. Gourdon P, et al. Crystal structure of a copper-transporting PIB-type ATPase. Nature. 2011; 475:59–64. [PubMed: 21716286]

16. Gonzalez-Guerrero M, Eren E, Rawat S, Stemmler TL, Arguello JM. Structure of the two transmembrane Cu+ transport sites of the Cu+-ATPases. J Biol Chem. 2008; 283:29753–9. [PubMed: 18772137]
17. Moller JV, Olesen C, Winther AM, Nissen P. The sarcoplasmic Ca2+-ATPase: design of a perfect chemi-osmotic pump. Q Rev Biophys. 2010; 43:501–66. [PubMed: 20809990]
18. Jardetzky O. Simple allosteric model for membrane pumps. Nature. 1966; 211:969–70. [PubMed: 5968307]
19. Shannon RD. Revised Effective Ionic-Radii and Systematic Studies of Interatomic Distances in Halides and Chalcogenides. Acta Crystallographica Section A. 1976; 32:751–767.
20. Huang Z, Tajkhorshid E. Identification of the third Na+ site and the sequence of extracellular binding events in the glutamate transporter. Biophys J. 2010; 99:1416–25. [PubMed: 20816053]
21. Renthal R. Buried water molecules in helical transmembrane proteins. Protein Sci. 2008; 17:293–8. [PubMed: 18096637]
22. Baginski ES, Foa PP, Zak B. Microdetermination of inorganic phosphate, phospholipids, and total phosphate in biologic materials. Clin Chem. 1967; 13:326–32. [PubMed: 6036717]
23. Gourdon P, Sitsel O, Karlsen JL, Moller LB, Nissen P. Structural models of the human copper P-type ATPases ATP7A and ATP7B. Biological Chemistry. 2012; 393:205–216. [PubMed: 23029640]
24. Barry AN, et al. The lumenal loop Met672-Pro707 of copper-transporting ATPase ATP7A binds metals and facilitates copper release from the intramembrane sites. J Biol Chem. 2011; 286:26585–94. [PubMed: 21646353]
25. Tadini-Buoninsegni F, et al. ATP dependent charge movement in ATP7B Cu+-ATPase is demonstrated by pre-steady state electrical measurements. FEBS Lett. 2010; 584:4619–22. [PubMed: 20965182]
26. Lewis D, et al. Distinctive features of catalytic and transport mechanisms in mammalian Ca2+ (SERCA) and Cu+ (ATP7A/B) ATPases. J Biol Chem. 2012
27. Hatori Y, et al. Intermediate phosphorylation reactions in the mechanism of ATP utilization by the copper ATPase (CopA) of Thermotoga maritima. Journal of Biological Chemistry. 2008; 283:22541–22549. [PubMed: 18562314]
28. Poulsen H, et al. Neurological disease mutations compromise a C-terminal ion pathway in the Na(+)/K(+)-ATPase. Nature. 2010; 467:99–102. [PubMed: 20720542]
29. Hollenstein K, Dawson RJ, Locher KP. Structure and mechanism of ABC transporter proteins. Curr Opin Struct Biol. 2007; 17:412–8. [PubMed: 17723295]
30. Raimunda D, Gonzalez-Guerrero M, Leeber BW 3rd, Arguello JM. The transport mechanism of bacterial Cu+-ATPases: distinct efflux rates adapted to different function. Biometals. 2011; 24:467–75. [PubMed: 21210186]
31. Waldron KJ, et al. Structure and Metal Loading of a Soluble Periplasm Cuproprotein. Journal of Biological Chemistry. 2010; 285:32504–32511. [PubMed: 20702411]
32. Hassani BK, Astier C, Nitschke W, Ouchane S. CtpA, a Copper-translocating P-type ATPase Involved in the Biogenesis of Multiple Copper-requiring Enzymes. Journal of Biological Chemistry. 2010; 285:19330–19337. [PubMed: 20363758]
33. Ward SK, Abomoelak B, Hoye EA, Steinberg H, Talaat AM. CtpV: a putative copper exporter required for full virulence of Mycobacterium tuberculosis. Mol Microbiol. 2010; 77:1096–110. [PubMed: 20624225]
34. Festa RA, Thiele DJ. Copper at the front line of the host-pathogen battle. PLoS Pathog. 2012; 8:e1002887. [PubMed: 23028306]
35. Petrek M, et al. CAVER: a new tool to explore routes from protein clefts, pockets and cavities. BMC Bioinformatics. 2006; 7:316. [PubMed: 16792811]
36. Diederichs K, Karplus PA. Improved R-factors for diffraction data analysis in macromolecular crystallography. Nat Struct Biol. 1997; 4:269–75. [PubMed: 9095194]
37. Schneider CA, Rasband WS, Eliceiri KW. NIH Image to ImageJ: 25 years of image analysis. Nat Meth. 2012; 9:671–675.

38. Petersen C, Moller LB. Control of copper homeostasis in Escherichia coli by a P-type ATPase, CopA, and a MerR-like transcriptional activator, CopR. Gene. 2000; 261:289–98. [PubMed: 11167016]
39. Gourdon P, et al. HiLiDe—Systematic Approach to Membrane Protein Crystallization in Lipid and Detergent. Crystal Growth & Design. 2011; 11:2098–2106.
40. Kabsch W. Automatic Processing of Rotation Diffraction Data from Crystals of Initially Unknown Symmetry and Cell Constants. Journal of Applied Crystallography. 1993; 26:795–800.
41. McCoy AJ, et al. Phaser crystallographic software. J Appl Crystallogr. 2007; 40:658–674. [PubMed: 19461840]
42. Adams PD, et al. PHENIX: a comprehensive Python-based system for macromolecular structure solution. Acta Crystallogr D Biol Crystallogr. 2010; 66:213–21. [PubMed: 20124702]
43. Emsley P, Cowtan K. Coot: model-building tools for molecular graphics. Acta Crystallogr D Biol Crystallogr. 2004; 60:2126–32. [PubMed: 15572765]
44. Joosten RP, Womack T, Vriend G, Bricogne G. Re-refinement from deposited X-ray data can deliver improved models for most PDB entries. Acta Crystallogr D Biol Crystallogr. 2009; 65:176–85. [PubMed: 19171973]
45. Jo S, Lim JB, Klauda JB, Im W. CHARMM-GUI Membrane Builder for Mixed Bilayers and Its Application to Yeast Membranes. Biophysical Journal. 2009; 97:50–58. [PubMed: 19580743]
46. Jorgensen WL, Chandrasekhar J, Madura JD, Impey RW, Klein ML. Comparison of Simple Potential Functions for Simulating Liquid Water. Journal of Chemical Physics. 1983; 79:926–935.
47. Sansom MS, Scott KA, Bond PJ. Coarse-grained simulation: a high-throughput computational approach to membrane proteins. Biochem Soc Trans. 2008; 36:27–32. [PubMed: 18208379]
48. Lomize MA, Lomize AL, Pogozheva ID, Mosberg HI. OPM: orientations of proteins in membranes database. Bioinformatics. 2006; 22:623–5. [PubMed: 16397007]
49. Humphrey W, Dalke A, Schulten K. VMD: Visual molecular dynamics. Journal of Molecular Graphics & Modelling. 1996; 14:33–38.
50. Kale L, et al. NAMD2: Greater scalability for parallel molecular dynamics. Journal of Computational Physics. 1999; 151:283–312.
51. Klauda JB, et al. Update of the CHARMM All-Atom Additive Force Field for Lipids: Validation on Six Lipid Types. Journal of Physical Chemistry B. 2010; 114:7830–7843.
52. Mackerell AD, Feig M, Brooks CL. Extending the treatment of backbone energetics in protein force fields: Limitations of gas-phase quantum mechanics in reproducing protein conformational distributions in molecular dynamics simulations. Journal of Computational Chemistry. 2004; 25:1400–1415. [PubMed: 15185334]
53. Grubmüller H, Heller H, Windemuth A, Schulten K. Generalized Verlet Algorithm for Efficient Molecular Dynamics Simulations with Long-range Interactions. Molecular Simulation. 1991; 6:121–142.
54. Darden T, York D, Pedersen L. Particle Mesh Ewald - an N.Log(N) Method for Ewald Sums in Large Systems. Journal of Chemical Physics. 1993; 98:10089–10092.
55. Essmann U, et al. A Smooth Particle Mesh Ewald Method. Journal of Chemical Physics. 1995; 103:8577–8593.
56. Ryckaert JP, Ciccotti G, Berendsen HJC. Numerical-Integration of Cartesian Equations of Motion of a System with Constraints - Molecular-Dynamics of N-Alkanes. Journal of Computational Physics. 1977; 23:327–341.
57. Miyamoto S, Kollman PA. Settle - an Analytical Version of the Shake and Rattle Algorithm for Rigid Water Models. Journal of Computational Chemistry. 1992; 13:952–962.
58. Feller SE, Zhang YH, Pastor RW, Brooks BR. Constant-Pressure Molecular-Dynamics Simulation - the Langevin Piston Method. Journal of Chemical Physics. 1995; 103:4613–4621.
59. Martyna GJ, Tobias DJ, Klein ML. Constant-Pressure Molecular-Dynamics Algorithms. Journal of Chemical Physics. 1994; 101:4177–4189.

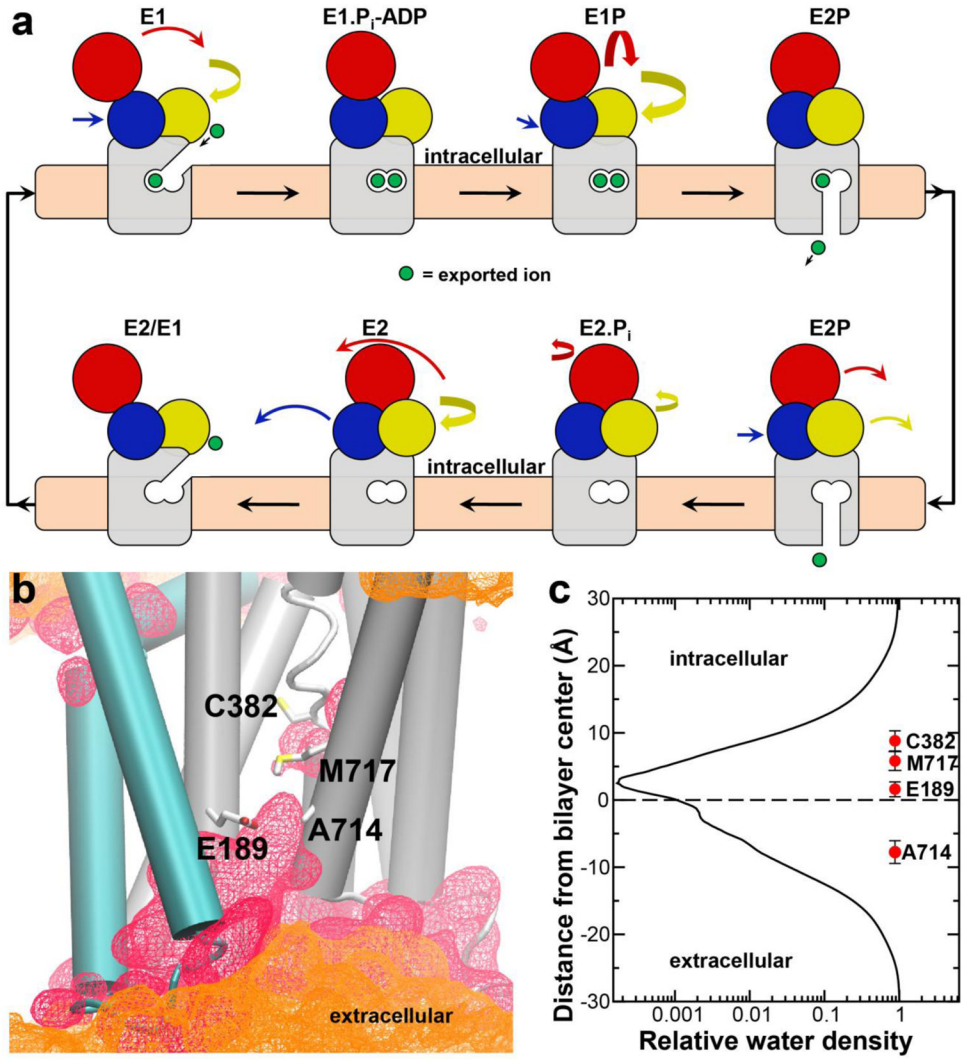

Figure 1. MD simulations suggest the E2.P$_i$ state to be open in CopA

a, Schematics of the classical P-type ATPase reaction cycle, known e.g. for Ca^{2+}-transporting SERCA. The intracellular A-, P- and N-domains are colored yellow, blue and red, respectively, while the M-domain is gray. Ions (two Ca^{2+} for SERCA, shown in green) are transported accompanied by phosphate hydrolysis and structural rearrangements (marked by arrows). Note that the transmembrane domain occludes upon initiation of dephosphorylation (E2.P$_i$). **b,** Average representation from the MD simulation of the CopA E2.P$_i$ state (pdb-id: 3RFU). The transmembrane domain is shown with helices MA-MB (Class-IB specific) and M1-M6 depicted in cyan and grey, respectively. The Cu^{+}-binding residues Cys382 and Met717 as well as Glu189 and Ala714Thr at the exit pathway are shown as sticks[16]. Lipid phosphates and water are shown as orange and red density surfaces at 5 % and 20 % occupancies, respectively (the fraction of presence in simulation frames). Water solvation reaches the ion binding residues. **c,** Density plot for the water distribution of the E2.P$_i$ MD simulation showing the number of water molecules relative to bulk solution along the membrane normal within 7 Å from the protein (intracellular side positive). The centers-of-mass with corresponding error bars are depicted for Cys382, Met717, Glu189 and Ala714. Cu^{+} must pass more than half of the membrane from the intramembanous ion-binding residues Cys382 and Met717 to be released to the extracellular side.

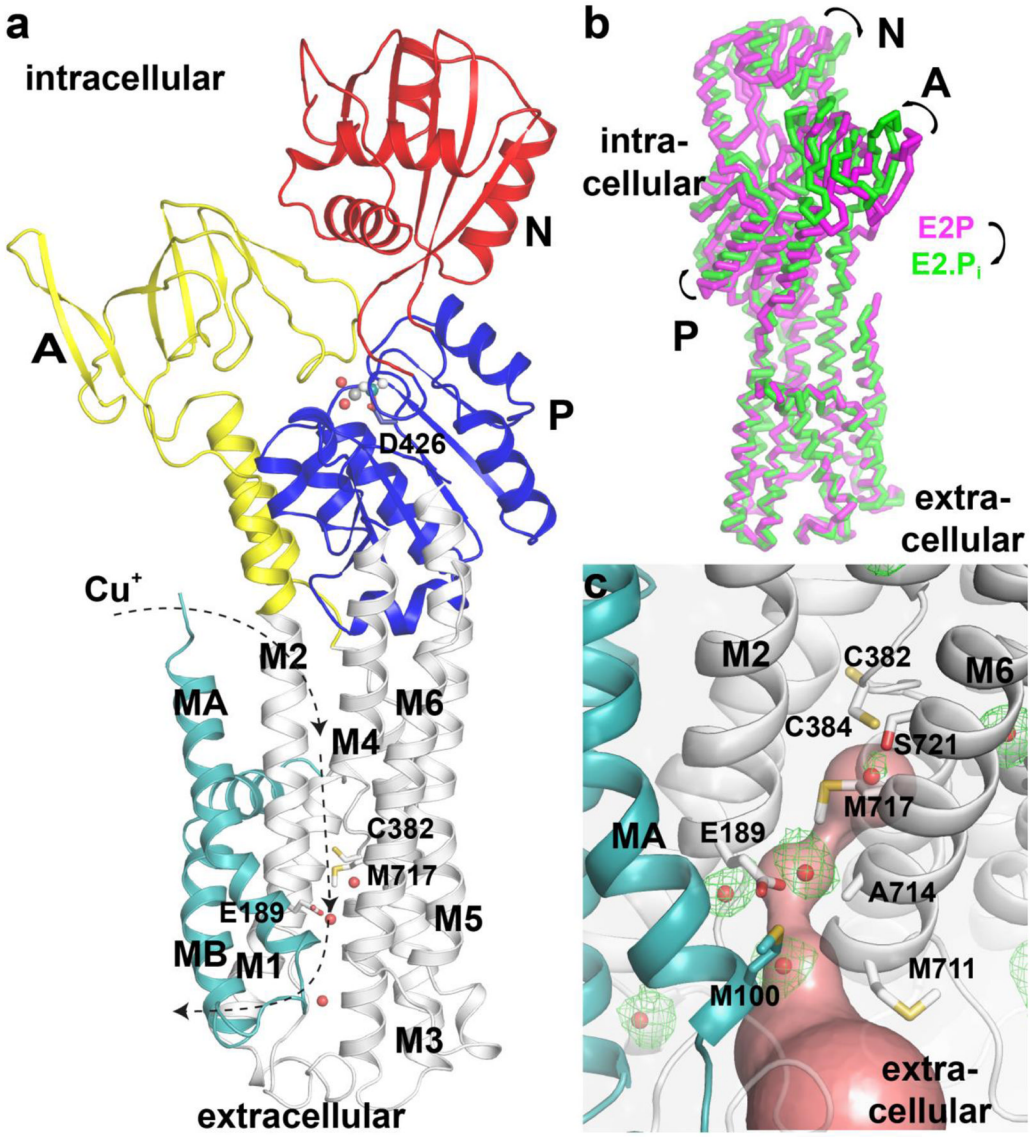

Figure 2. Crystal waters of the E2-BeF_3^- structure support the copper release pathway

The domains are colored as in Fig. 1a. **a,** The E2-BeF_3^- structure determined in this work. Black arrows mark the Cu^+ transport direction. Crystal waters located in close vicinity to Cys382, Met717, Glu189 and Ala714 are shown as red spheres. **b,** Superimpositions of the TM domains of the E2P (purple) and E2.P_i (green) states of LpCopA. Intracellular domains change their configuration from the E2P to the E2.P_i state (black arrows) while the TM domains remain rigid. **c,** Close-up of the extrusion pathway with residual F_{obs}-F_{calc} electron density (green mesh at 2.5σ, prior to modeling) of BeF_3^--bound LpCopA with key residues labeled. The opening from the Cu^+ high-affinity coordinating residues Cys382, Cys384 and Met717 found in the E2P conformation found using the software CAVER[35] is shown as a red surface and overlays with crystallographic water molecules shown as red spheres.

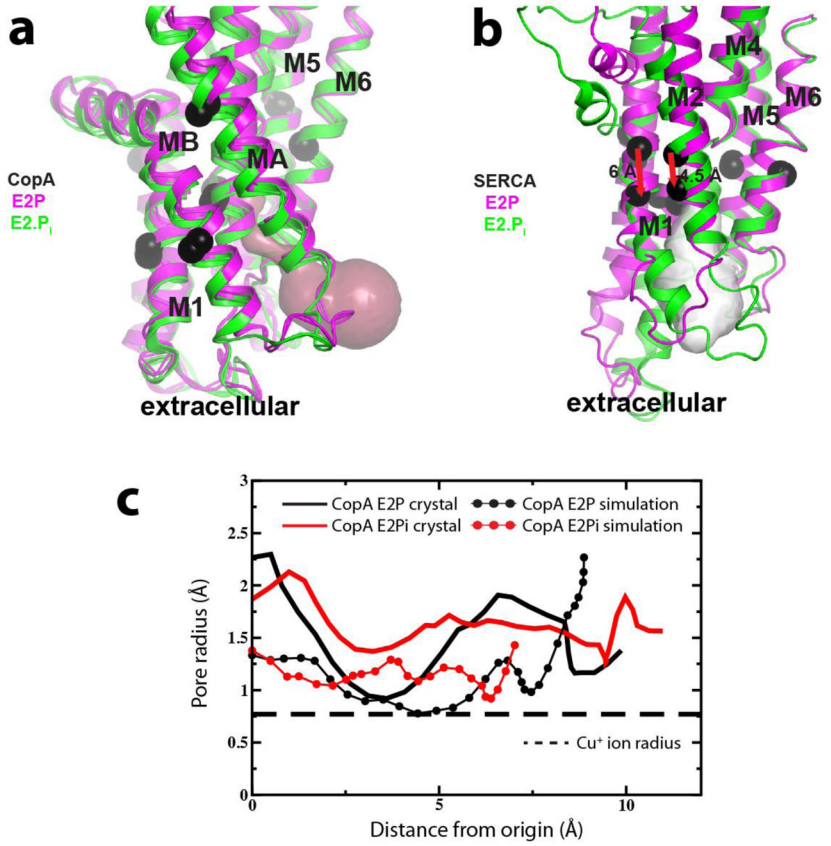

Figure 3. The CopA release pathway is unique and able to accommodate Cu^+ ions

a, View of the transmembrane domains of the E2P (purple) and E2.P_i (green) structures of SERCA and its release pathway (white). Black spheres indicate the movements of one Cα atom in each helix and transmembrane helices M7-M10 have been removed for clarity. Significant shifts of helices M1-M2 and M3-M4 occlude SERCA in the E2P to E2.P_i. See also Supplementary Fig. 4a. **b,** Equivalent view as in panel d for CopA with its release pathway (purple) showing that CopA remains rigid in the E2P to E2.P_i transition. See also Supplementary Fig. 4b. **c,** Pore radii of the E2P and E2.P_i crystal structures and average structures from last 10 ns of the corresponding simulations compared to the size of Cu^+. The origin was set close to the centers-of-mass of the internal Cu^+ coordinators Cys382, Cys384 and Met717. See Supplementary Fig. 10 for methods specification and corresponding SERCA analyses.

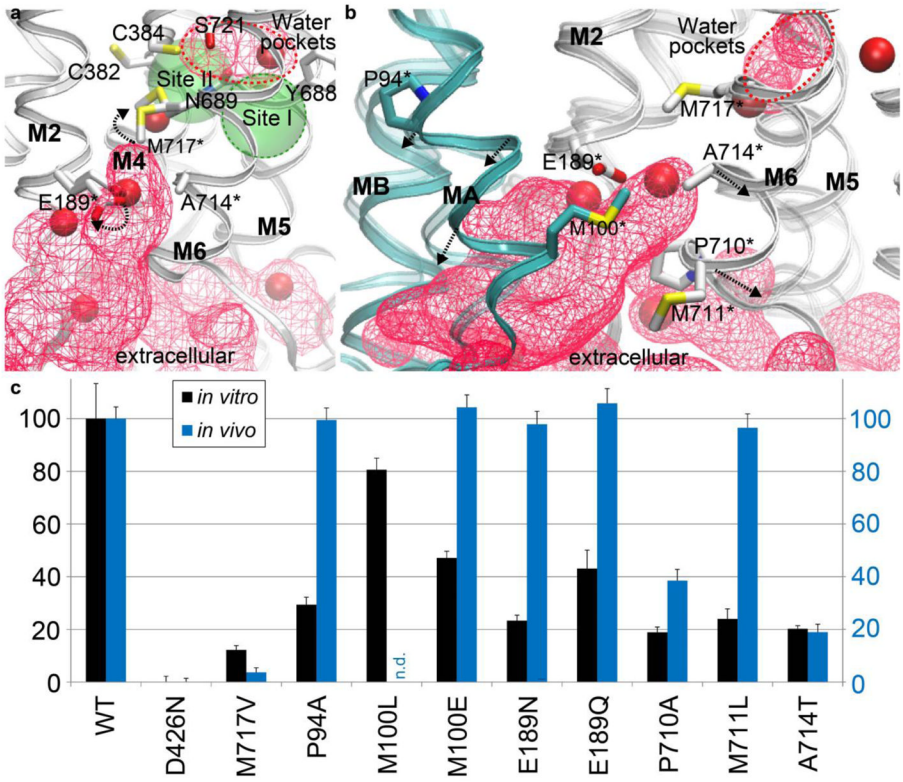

Figure 4. Copper transfer from the high-affinity binding sites and the extracellular release pathway

Hydration and sidechain dynamics of the LpCopA crystal structures colored as in Fig. 1a and with E2P crystal waters shown as solid, red spheres. Residues included in the functional analysis summarized in Fig. 4c are marked by asterisks. **a,** The E2P state simulation. Crystallographic and simulated (averaged over the last 20 ns) sidechain configurations are shown for Met717 and Glu189, while the E2:BeF_3^- crystal structure represents Cys382, Cys384, Tyr688, Asn689, Ala714 and Ser721 as they do not rearrange significantly during simulations. Green transparent spheres represent the approximate locations of calcium sites of SERCA (pdb-id: 3BA6), with Site I encircled in green, compared to the equivalent water pockets (shown as in Fig. 1a and encircled in red). Note that a bulk water pathway associates Glu189 with the extracellular environment. The intrinsic flexibility of Met717 and Glu189 suggests a shuttling role in Cu^+-transfer. See also Supplementary Fig. 8. **b,** An average from the last 20 ns of the E2.P_i simulation (transparent) superimposed on the E2.AlF_4^- (pdb-id: 3RFU) crystal structure (solid), highlighting the opening in CopA, which involves the class-specific helix MA and common P-type ATPase core helices M2 and M6 and emerges from Pro94 and Pro710. Arrows mark movements of Cα atoms in MA and M6 (shown as cyan and grey spheres, analysis described in Supplementary Fig. 16). The red circle is equivalent to the one in panel a. **c,** Relative *in vitro* activity of LpCopA copper release pathway mutants as compared to wild-type (WT) protein and the inactive Asp426Asn mutant (black). Relative *in vivo* susceptibility for copper of the same mutations (blue, see also Supplementary Fig. 19), except for M100L, which was not cloned for the *in vivo* assay.

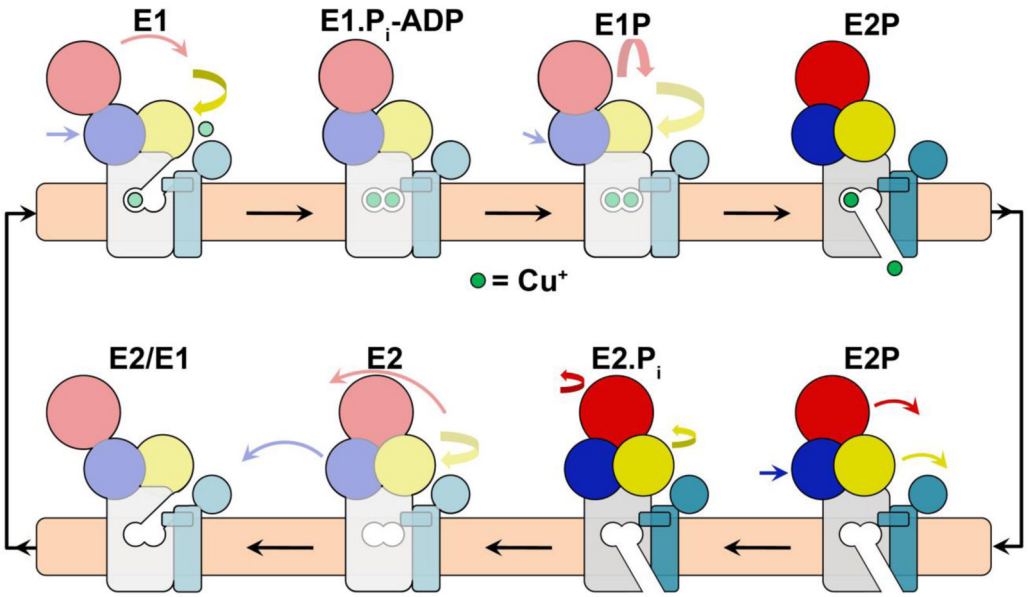

Figure 5. Mechanistic implications of the open E2.P$_i$ state

a) The CopA domains are colored as in Fig. 1a and colored arrows indicate the coming movements of the corresponding domain to the following conformation. In contrast to the well-characterized Ca^{2+}-P-type ATPase SERCA[17], no major movements are identified between the transmembrane domains of the E2P and E2.P$_i$ LpCopA states, indicating a class-specific transport mechanism with an open release pathway associated with dephosphorylation.

Table 1

Data collection, phasing and refinement statistics.

Data statistics (XDS)[a]		
Beamline	ESRF ID 29	ESRF ID 29
Wavelength (Å)	0.9763	0.9763
Space group	C2	$P2_12_12_1$
Unit-cell parameters	a = 242.0 Å, b=71.4 Å, c= 72.4 Å α = 90°, β = 100.01 °, γ = 90°	a = 73.0 Å, b=85.0 Å, c= 342.4 Å α = β = γ = 90°
Resolution range (Å)	48.2 – 2.7 (2.8 – 2.7)	85.6 – 7.11 (7.3 – 7.11)
Total unique reflections	32589 (3248)	3525 (255)
Multiplicity	7 (7.2)	12.5 (12.2)
Completeness (%)	96.6 (94.1)	98.7 (99.6)
R_{merge}[b]	12.3 (96.7)	27.8 (125.6)
<I/σ(I)>	21.27 (2.04)	7.9 (3.5)
Wilson B factor	68.3	n.a.
Phasing statistics (PHASER)		
Method	Molecular replacement[c]	Molecular replacement
Fast rotation Z score	7.5	5.7
Fast translation Z score	8.7	9.4
Packing clash score	9	0
LLG	131	408
Refinement statistics (PHENIX)		
Resolution range (Å)	48.2 – 2.75 (2.81 – 2.75)	85.6 – 7.1
No. of reflections	30867 (1718)	3468
R_{work}	0.199 (0.405)	30.5
No. of reflections for R_{free}	2264 (116)	
R_{free}	0.247 (0.465)	
R.m.s.d. bonds (Å)	0.010	
R.m.s.d. angles (°)	1.23	
No. of protein atoms	4945	
No. of ligand atoms	92	
No. of solvent atoms	59	
Overall average B factor (Å^2)	63.7	
Model statistics[d]		
Residues in favored region (%)	96.2	
Residues in allowed region (%)	3.0	
Residues in non-favored region (%)	0.8	
Rotamer outliers (%)	2.1	
Clash score	23.8	

[a] Outer shell statistics in parentheses.

[b] Calculation according to 36.

[c] Data processed to 2.9 Å have been used for this.

[d] Molprobity statistics calculated by phenix.refine.